La$_{1-x}$K$_x$FeO$_{3-\delta}$: An Anion Intercalative Pseudocapacitive Electrode for Supercapacitor Application

Rakesh Mondal, Neeraj Kumar Mishra, Thandavarayan Maiyalagan, Asha Gupta, and Preetam Singh*

Read Online

ACCESS | Metrics & More | Article Recommendations | SI Supporting Information

ABSTRACT: The green energy alternative to a fossil fuel-based economy can be provided only by coupling renewable energy solution solutions such as solar or wind energy plants with large-scale electrochemical energy storage devices. Enabling high-energy storage coupled with high-power delivery can be envisaged though high-capacitive pseudocapacitor electrodes. A pseudocapacitor electrode with multiple oxidation state accessibility can enable more than $1e^-$ charge/transfer per molecule to facilitate superior energy storage. K-doped LaFeO$_3$ (La$_{1-x}$K$_x$FeO$_{3-\delta}$) is presented here as an electrode having a high pseudocapacitance storage, equivalent to $1.32e^-$ charge/transfer per molecule, resulting in a capacity equivalent of 662 F/g at 1 mV/s scan rate by introduction of a layered potential over the Fe-ion octahedral to utilize higher redox state energies (Fe^{4+}→ Fe^{2+}). La/K ordering in orthorhombic perovskite (La$_{1-x}$K$_x$FeO$_{3-\delta}$) made the Fe^{4+} oxidation state accessible, and a systematic shift in the redox energies of Fe$^{4+/3+}$ and Fe$^{3+/2+}$ redox couples was observed with K$^+$ ion doping in the A site of the LaFeO$_3$ perovskite, which resulted in a high faradic contribution to the capacitance, coupled with anionic intercalation of H$_2$O/OH$^-$ in the host perovskite lattice. The surface capacitive and diffusion control contributions for capacitance are about 42 and 58%, respectively, at −0.6 V, with a scan rate of 1 mV/s. A high gravimetric capacitance, equivalent to 619, 347, 188, 121, and 65 F/g, respectively, at 1, 2, 3, 5, and 10 A/g constant current, was observed for the La$_{0.5}$K$_{0.5}$FeO$_{3-\delta}$ electrode. Up to 88.9% capacitive retention and 97% Coulombic efficacy were obtained for continuous 5000 cycles of charge/discharge for the La$_{0.5}$K$_{0.5}$FeO$_{3-\delta}$ electrode. The gravimetric capacitance values of ASCs (activated carbon//La$_{0.5}$K$_{0.5}$FeO$_{3-\delta}$) are 348, 290, 228, and 147 F/g at current densities of 1, 2, 3, and 5 A/g, respectively. A maximum specific power of ∼3594 W/kg was obtained when the specific energy reached ∼117 Wh/kg at 5 A/g of current density.
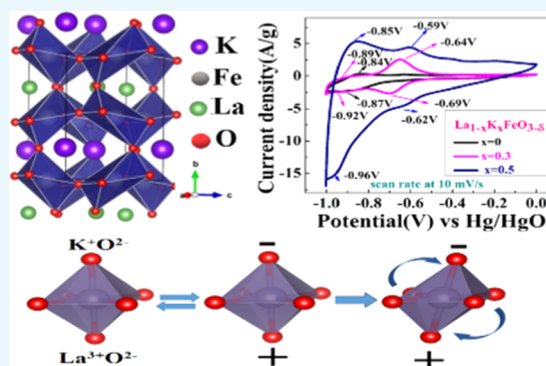
1. INTRODUCTION

To move away from fossil fuel-based energy solution and to produce power and electricity through the renewable energy generated through sources like solar, wind, and tidal energy, a large-scale electrochemical energy storage system is required.[1,2] Electrochemical energy storage devices such as batteries and electrochemical capacitors are empowering portable electronics and broad-range electricity transmission through grid regulation and the transport sector.[3] An electrochemical cell is generally made of two electrodes separated by an electrolyte (a high-ionic conductor made of aqueous and nonaqueous materials). As per the charge storage mechanism, electrochemical energy storage (EES) systems are classified into three categories: (a) electric double-layer capacitors (EDLCs) (containing carbon-based material, due to its high conductivity and high surface area available to adsorb electrolyte ions onto the surfaces to form an electric double-layer charge storage through electrified material[4,5]); (b) batteries (storing electrical energy as chemical energy in two electrodes: a reductant (anode) and an oxidant (cathode), separated by an electrolyte that allows transport of the ionic component of the chemical reaction for storage inside the electrode materials[6]); (c)

pseudocapacitors (in addition to having an electrostatic electric double layer, they store electrical energy in a faradic component, resulting normally from a shallow insertion of the mobile ions of the electrolyte into an electrode host with the reduction of host-electrode cations[7]). The E vs t plot behavior for the EDLC (surface charge storage) is linear, for the battery (faradic reaction) it is nonlinear, and for the pseudocapacitor (combination of faradic and surface charge storage) it is more linear compared to the battery.[8,9] RuO$_2$ was the first extensively studied material to show pseudocapacitance behavior and continues to be an excellent capacitance material due to its high chemical stability and conductivity.[10] However, its scarcity and high cost limit its application for commercial purposes, and as an alternate, MnO$_2$ was

demonstrated to possess pseudocapacitive behavior.[11] Vigorous studies have started on transition metal oxide-based materials such as NiO, V_2O_5, spinel Co_3O_4, Fe_2O_3, and mixed spinel $NiCo_2O_4$ to explore them as electrodes of a pseudocapacitor.[12–18] Perovskite-type $LaMnO_3$ was demonstrated as an anion-intercalation pseudocapacitor.[19] Perovskite oxides have the unit cell formula ABO_3, where the A-site is either an alkaline or lanthanide element, while the B-site is a transition metal element. By strategically selecting the A-site elemental composition, one can readily control the B-site element's oxidation state as well as the overall oxygen vacancy content via charge compensation.[20,21] Perovskite supercapacitors have attracted widespread attention, and several perovskites such as $LaNiO_3$,[22] $LaFeO_3$,[23] $La_xSr_{1-x}CoO_{3-\delta}$,[24] $La_xSr_{1-x}Cu_{0.1}Mn_{0.9}O_{3-\delta}$,[25] $Sr_2CoMoO_{6-\delta}$,[26] and $La_{0.85}Sr_{0.15}MnO_3$[27] were investigated for pseudocapacitance applications.

Perovskites are a very important class of electronic materials, especially layered perovskites such as $YBa_2Cu_3O_7$,[28] $La_{2-x}Ba_xCuO_4$,[29] $LaCsNb_2O_7$,[30] and $LaKNb_2O_7$.[30] $YBa_2Cu_3O_7$ crystallizes in orthorhombic perovskite structure, where an alternate layer of Y and Ba induces an interplanar potential that generates cooper pairs, and stabilizes the Cu^{3+} ion in the B-site octahedral responsible for the high-temperature superconducting properties of the materials. The effect of internal field was also presented in the layered perovskite $NaLnTiO_4$ (Ln = Y, La–Tb), where the internal potential generated over the Ti octahedral resulted in a systematic shift in the redox energy of $Ti^{4+/3+}$ couples.[31] Similarly, here, we envisaged the concept of accessing higher redox energies though incorporation of an internal layer potential to achieve multiple electron transfer, such as $Fe^{4+} \rightarrow Fe^{2+}$, for higher pseudocapacitive energy storage. In this manuscript, we have investigated the concept of layered potential on a transition metal-ion octahedral to utilize high redox energies (higher oxidation states such as $Fe^{4+/2+}$) for fabrication of high-capacity electrodes. Using La/K ordering in orthorhombic perovskite ($La_{1-x}K_xFeO_{3-\delta}$), the Fe^{4+} oxidation state is accessed and a systematic shift in redox energy ($Fe^{4+/3+}$ and $Fe^{3+/2+}$) with K^+ ion doping on the A site of $LaFeO_3$ perovskite is shown, and in turn, a high pseudocapacitance of the electrode is demonstrated. A specific capacitance of 662 F/g, equivalent to $1.32e^-$/mole charge transfer, was observed for $La_{0.5}K_{0.5}FeO_{3-\delta}$ in aqueous 2 M KOH electrolyte in a voltage window of 1 V. The detailed synthesis, characterizations, and electrochemical performance of $La_{1-x}K_xFeO_{3-\delta}$ are presented in this manuscript.

2. EXPERIMENTAL DETAILS

2.1. Materials Synthesis and Characterizations. The solid-state ceramic synthesis route was utilized to synthesize crystalline K-doped $La_{1-x}K_xFeO_{3-\delta}$ (x = 0, 0.1, 0.2, 0.3, 0.4, 0.5) because this route in general produces more thermodynamically stable compounds. La_2O_3 (99.9%), K_2CO_3 (99.9%), and Fe_2O_3 (99.9%) were taken as precursors for the synthesis of the materials. The precursors were taken in stoichiometric ratio and mixed in an agate mortar pestle for about 30 min. The mixture was then fired in a platinum crucible at 1050 °C for 12 h for the preparation of $LaFeO_3$ and at 1150 °C for 12 h for the preparation of $La_{1-x}K_xFeO_{3-\delta}$ (x = 0.1, 0.2, 0.3, 0.4, 0.5), followed by slow cooling to room temperature. Multiple heating and grinding of the samples were carried out to get single-phase materials. The phase formation was studied using

a Rigaku Miniflex desktop X-ray diffractometer (XRD) with Cu Kα radiation (λ = 1.54 Å) in the range $2\theta \sim 20–90°$ with a step size of 0.02°. The structures were refined by the Rietveld refinement method using FULLPROF suite software, and orthorhombic perovskite (*Pnma*, space group 62) was taken as the model structure. The microstructures of the sintered samples were investigated using a scanning electron microscope (EVO—Scanning Electron Microscope MA15/18). The average grain size was calculated using the linear intercept method with ImageJ software. Pore-size distribution and specific surface area of the sample were measured by BET (MicrotracBEL).

X-ray photoelectron spectroscopy (XPS) studies were carried out to investigate the electronic structures of the materials. XPS of the sample was carried out using a Thermo Scientific Multilab 2000 instrument with Al Kα radiation operated at 150 W. The binding energies reported here are with reference to C (1s) at 284.5 eV, and they are accurate within ±0.1 eV. The oxidation state of Fe and oxygen stoichiometry were determined by chemical analysis using a redox titration method called iodometry. Twenty milligrams of active materials was dissolved in 30 mL of hydrochloric acid (3 M) in the presence of 24 mg of potassium iodide (KI), and the liberated iodine was titrated with sodium thiosulfate $Na_2S_2O_3$ (1 M) using starch as indicator. Concordant results for oxygen stoichiometry were obtained within an error of ±0.01. High-purity argon gas was bubbled into the solution to avoid oxygen contamination from air, and double-distilled preheated water was used in titration to avoid any dissolved oxygen contamination and active bacteria present in the water.

2.2. Electrochemical Studies. The electrochemical measurements were carried out using NOVA 2.0 autolab. The catalyst ink was prepared by homogenizing 35 mg of catalyst, 10 mg of acetylene black, and 5 mg of PVDF binder in 1 mL of NMP solvent under an ultrasonication bath for 40 min. To investigate the activity of the supercapacitance, an aliquot of 20 μL of homogenized ink was deposited by a micropipette onto the surface of a carbon paper (torry carbon paper, alfa Aesar) (1 cm × 1 cm area) and dried under an IR lamp. The electrode loading was calculated by taking the weight of the electrode using an electronic balance (error limit: 0.01 mg). For that, first, the weight of the Torrey paper was taken; then, the weight of the coated electrode (after drying the coated ink on Torrey carbon paper of 1 × 1 cm² area) was taken for the study. Then, from the difference in the weights, the exact loading of the electrode material was calculated. The total material load was typically 1 mg (0.7 mg active material/carbon/PVDF binder).

Cyclic voltammetry (CV), galvanometric charge/discharge, and electrochemical impedance spectroscopy (EIS) in a conventional three-electrode arrangement were used to determine the electrochemical characteristics of the prepared pseudocapacitor by a Metrohm Autolab (PGSTAT204) equipped with FRA32M module. Electrochemical measurements were analyzed using NOVA 2.0 software.

Pt was used as the counterelectrode and Hg/HgO (1 M KOH) was utilized as the reference electrode. All electrodes were measured in 2 M KOH electrolyte; cyclic voltammetry (CV) was used to show redox behavior; chronopotentiometry was used for charge–discharge capacity measurements; and EIS was employed for the overall internal resistance measurements.
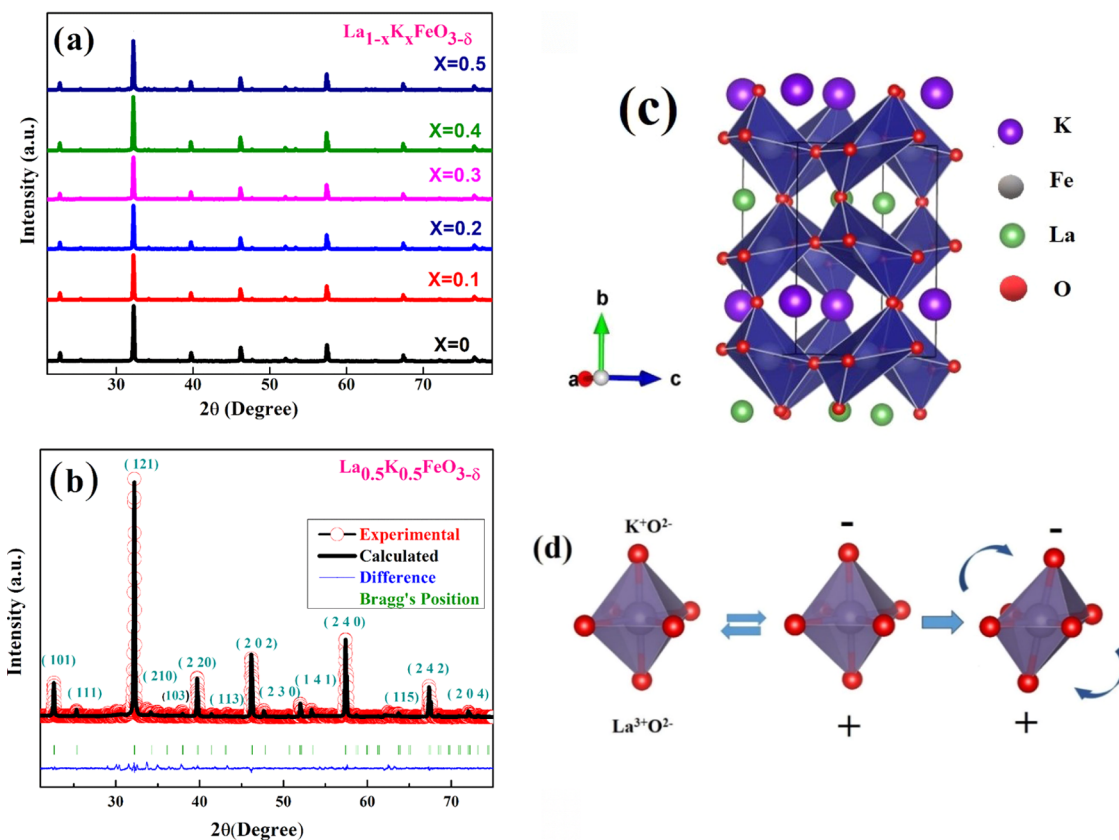
Figure 1. (a) XRD pattern of $La_{1-x}K_xFeO_{3-\delta}$ (x = 0, 0.1, 0.2, 0.3, 0.4, 0.5), (b) Rietveld refinement of $La_{0.5}K_{0.5}FeO_{3-\delta}$, (c) structure of $La_{0.5}K_{0.5}FeO_{3-\delta}$, and (d) Jahn−Teller distortion over Fe−O octahedra in orthorhombic $La_{0.5}K_{0.5}FeO_{3-\delta}$ structure.
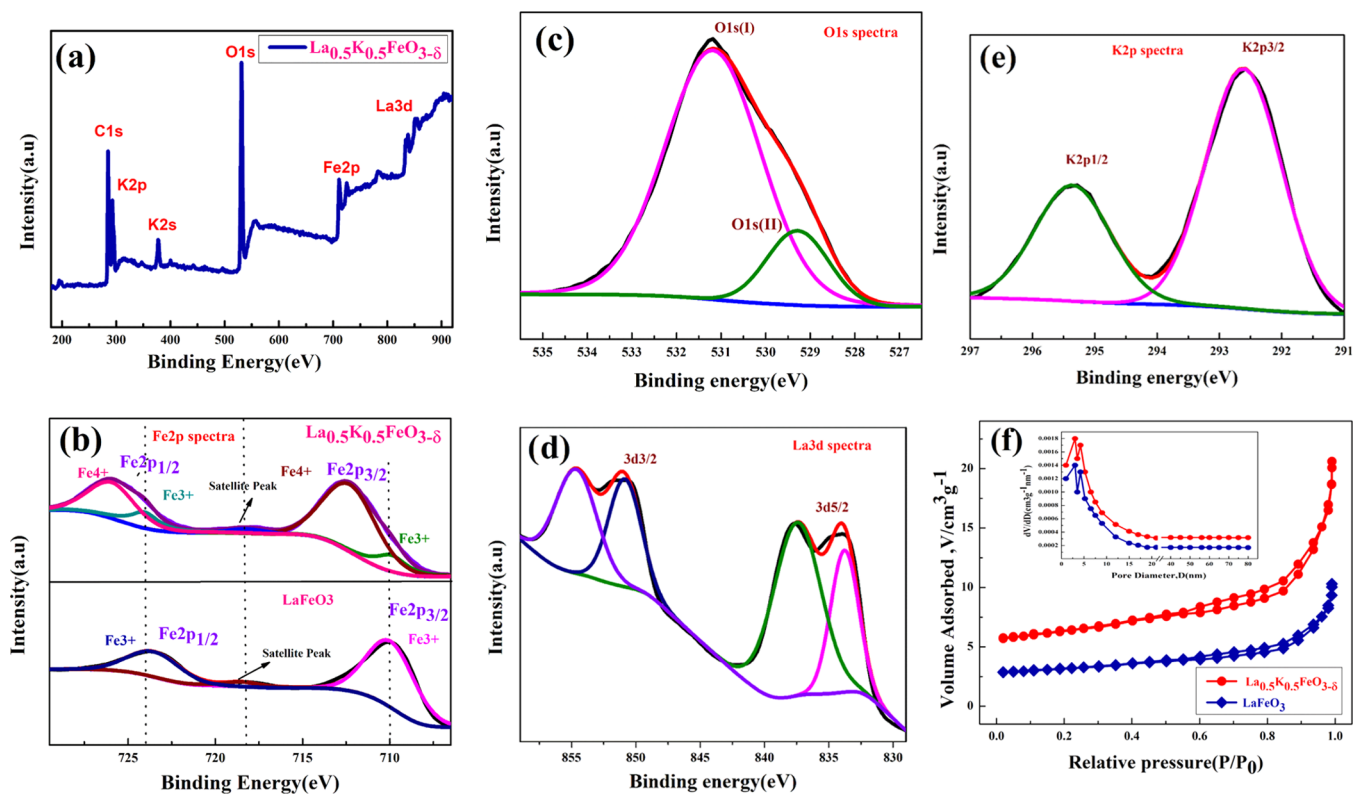

Figure 2. XPS of $La_{0.5}K_{0.5}FeO_{3-\delta}$ of the powder sample: (a) full survey, (b) Fe (2p) core level, (c) O (1s), (d) La (3d), and (e) K (2p). (f) N_2 adsorption−desorption isotherms with pore-size distribution.

3. RESULTS AND DISCUSSION

The XRD pattern of the prepared materials treated at 1150 °C for 12 h is shown in Figure 1a for $La_{1-x}K_xFeO_{3-\delta}$ (x = 0, 0.1, 0.2, 0.3, 0.4, 0.5). All of the synthesized materials show a single-phase formation. The prominent single-phase diffraction peak matches well with JCPDS file: 1526450. The Rietveld refined XRD profile of $La_{0.5}K_{0.5}FeO_{3-\delta}$ is provided in Figure 1b. Rietveld refinement studies of $La_{1-x}K_xFeO_{3-\delta}$ (x = 0, 0.1, 0.2, 0.3, 0.4, 0.5) show that all materials adopted an orthorhombic (*Pnma*, space group 62) type structure. The structure parameters derived from Rietveld refinement are presented in Table S1 (Supporting Information). Figure S1 (Supporting Information) shows that the (002) peak (highest-intensity peak) shifted linearly to a lower 2θ value with increasing dopant (K) concentration on the La site. As the ionic radii of K^+ (1.64 Å, 12 coordination) is greater than that of La^{3+} (1.36 Å, 12 coordination),[32] doping of K on the La site will result in the peak shifting to a lower 2θ value. In the orthorhombic cell, large percentages of La ion were replaced by K ion; this may have resulted in the formation of the La and K alternating layer as shown in Figure 1c. The alternating layer of La and K can build a charge potential over the Fe−O octahedra, resulting in a tilt in the bond angle, and elongation in the nonplanar bonding, resulting in a Jahn−Teller type structural distortion of the Fe−O octahedral as shown in Figure 1d (vista image). This distortion favors the in situ formation of Fe^{4+} (electronic configuration: $t_{2g}^3e_g^1$) to support the Jahn−Teller distortion. Thus, this internal potential affects or shifts the redox energy of Fe in such a way that $Fe^{4+/3+}$ and $Fe^{3+/2+}$ redox couples can become accessible to facilitate the superior pseudocapacitive storage capacity of the materials.

The survey spectra of the $La_{0.5}K_{0.5}FeO_{3-\delta}$ sample containing (C 1s), O (1s), Fe (2p), La (3d), K (2s) (377.41 eV),[33] and K (2p) (293.16 eV)[33] are shown in Figure 2a. To investigate the Fe oxidation state, XPS of the core-level Fe (2p) spectra of $La_{0.5}K_{0.5}FeO_{3-\delta}$ and $LaFeO_3$ samples is shown in Figure 2b. The XPS curve is fitted or deconvoluted with the help of XPSPEAK41 software. The peak position indicates that only the Fe^{3+} state is present in $LaFeO_3$ and both Fe^{3+} and Fe^{4+} states are present in $La_{0.5}K_{0.5}FeO_{3-\delta}$. For the Fe^{3+} oxidation state, binding energies were obtained at 709.95 eV ($2p_{3/2}$) and 723.74 eV ($2p_{1/2}$), and for the Fe^{4+} oxidation state, binding energies were obtained at 712.65 eV ($2p_{3/2}$) and 726.2 eV ($2p_{1/2}$) with the presence of a weak satellite peak at 718.40 eV.[34] The Fe ($2p_{3/2,1/2}$) spectra clearly depict the presence of Fe^{4+} ion as the majority phase in $La_{0.5}K_{0.5}FeO_{3-\delta}$. The ratio of Fe^{4+} and Fe^{3+} ions was calculated from their peak strength and was found to be 85:15 in the materials. Figure 2c shows the O (1s) spectra of the $La_{0.5}K_{0.5}FeO_{3-\delta}$ sample containing two binding energies, respectively, at O 1s(I) (531.16 eV) and O 1s(II) (529.27 eV) due to bonding with two distinctive Fe^{4+} and Fe^{3+} ions present in the materials. Figure 2d shows the La (3d) spectra presenting two sets of La $(3d)_{5/2}$ and La $(3d)_{1/2}$ peaks at (833.75 and 850.77 eV) and (837.49 and 854.51 eV), respectively, due to its bonding with two different types of Fe−O octahedral. Figure 2e shows K (2p) 3/2 and 1/2 spectra at 293.59 and 295.36 eV, respectively.

N_2 adsorption−desorption isotherms with pore-size distribution are shown for $LaFeO_3$ and $La_{0.5}K_{0.5}FeO_{3-\delta}$ in Figure 2f. The surface area for pure $LaFeO_3$ was found to be 19 m^2/g, and for $La_{0.5}K_{0.5}FeO_{3-\delta}$ sample it was 26 m^2/g. Both samples show a large number of pores with a pore-size distribution

between 2 and 12 nm diameter. Iodometry titrations were carried out to determine the oxygen stoichiometry of the $La_{0.5}K_{0.5}FeO_{3-\delta}$ sample, and the oxygen content was found to be close to 2.92 ± 0.01. This suggests that the $La_{0.5}K_{0.5}FeO_{2.92}$ sample contains 84% of Fe^{4+} and 16% of Fe^{3+}. This study matches very well with the XPS study of the Fe oxidation state of our sample. Similarly, for the $La_{0.7}K_{0.3}FeO_{3-\delta}$ sample, Fe^{4+}/Fe^{3+} oxidation states were found to be in the ratio of 54:46, and the oxygen content was found to be 2.97.

The scanning electron microscope (SEM) image shown in Figure 3a presents the porous sphere-type particle morphology
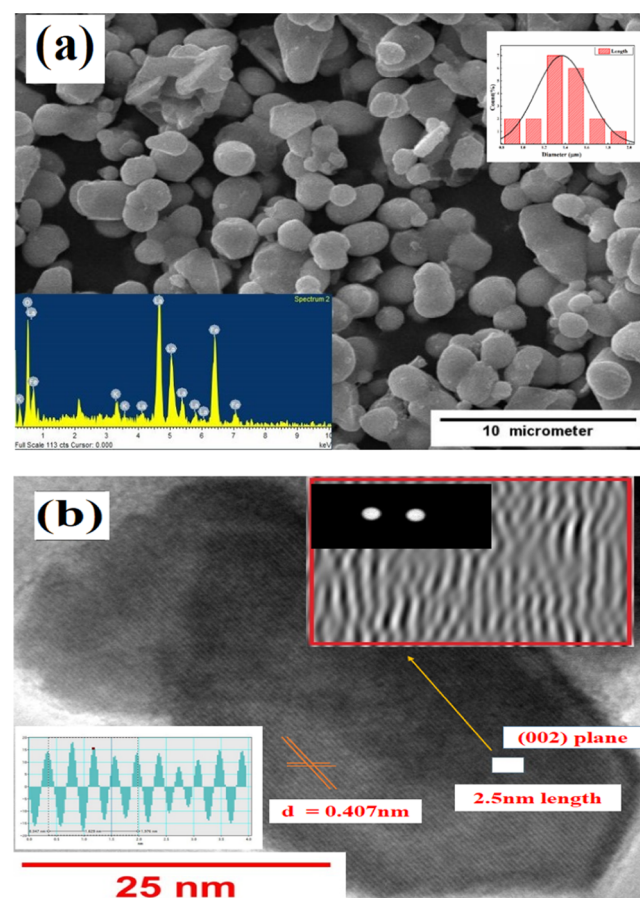

Figure 3. (a) SEM image showing the morphology characteristics of $La_{0.5}K_{0.5}FeO_{3-\delta}$ and particles' distribution from the SEM image; (b) HRTEM image comprising the plane with distorted fringes (inset: FFT and inverse FFT of the selected region) and line profile of the (002) plane. The selected line is the inverse FFT image of the super structural peak region.

of the $La_{0.5}K_{0.5}FeO_{3-\delta}$ sample. Particle-size distribution was calculated using ImageJ software and was fitted with Gaussian distribution. The particles' diameters were found to be in the range of 0.856−1.38 μm, with an average particle diameter of about 1.3 μm. Figure 3b shows the high-resolution transmission electron microscopy (HRTEM) images of the sample. Lattice fringes are clearly visible in the inverse fast Fourier transform (FFT) (mapping with Gatan Digital micrograph software) of this region, confirming the crystalline nature of $La_{0.5}K_{0.5}FeO_{3-\delta}$. The lattice fringe spacing is in agreement with the interplanar spacing obtained from the XRD results.

The electrochemical performance of $La_{1-x}K_xFeO_{3-\delta}$ (x = 0, 0.3, 0.4, 0.5) samples was determined from the cyclic
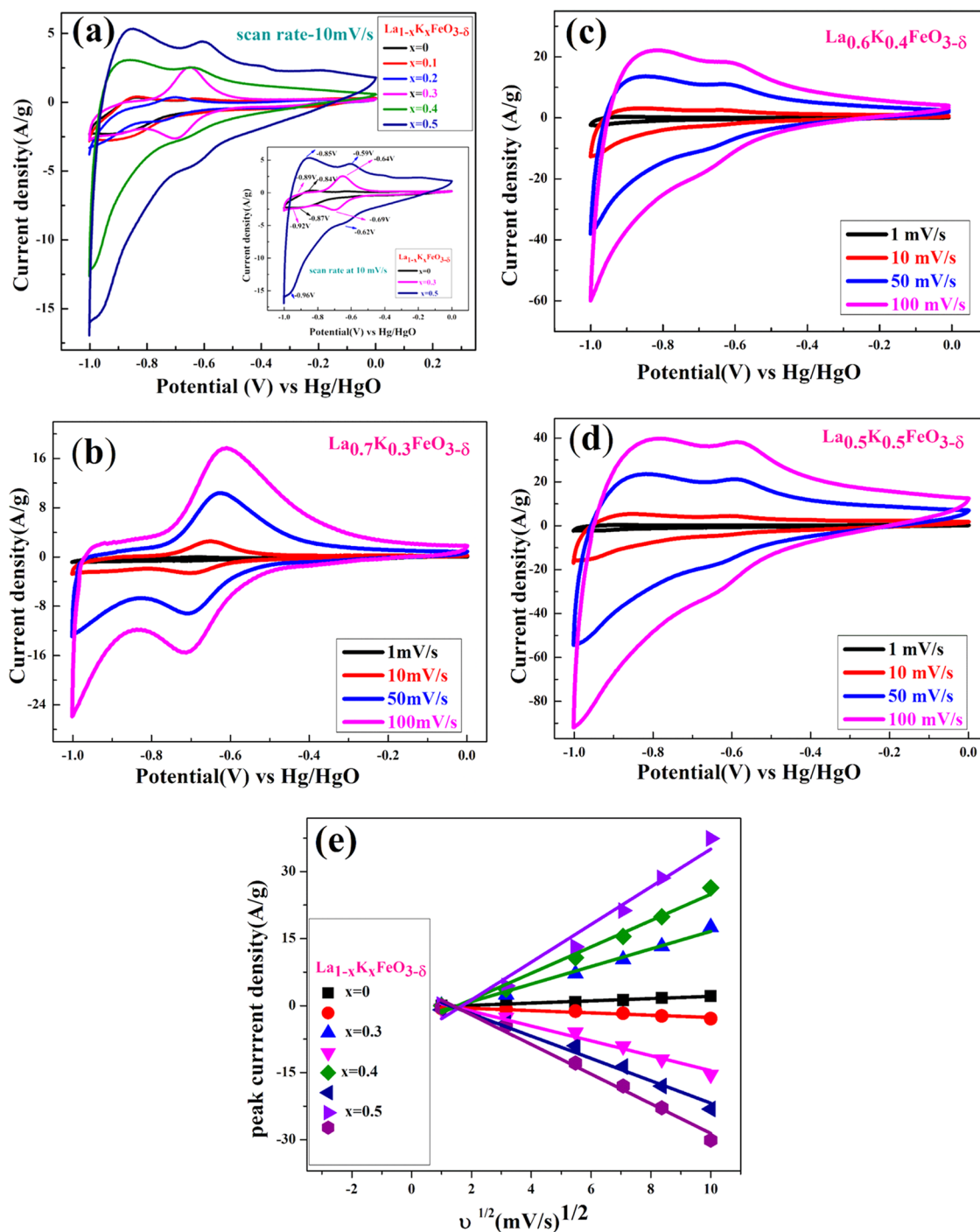
Figure 4. (a) Cyclic voltammetry of $La_{1-x}K_xFeO_{3-\delta}$ (x = 0, 0.4, and 0.5) material at a scan rate of 10 mV/s in 2 M KOH electrolyte; (b−d) cyclic voltammetry of $La_{1-x}K_xFeO_{3-\delta}$ (x = 0.3, 0.4, 0.5) material in 2 M KOH electrolyte; and (e) plot of peak current density vs square root of the scan rates of the $La_{1-x}K_xFeO_{3-\delta}$ (x = 0, 0.3, 0.5) sample.

voltammetry and galvanistic charge/discharge curve. All samples of $La_{1-x}K_xFeO_{3-\delta}$ (x = 0, 0.3, 0.4, 0.5) were studied in a 2 M KOH electrolyte in the voltage range of 0 to −1 V. We performed the study up to −1 V because below that we observed oxygen reduction reaction (ORR) over our electrode, which creates loss of capacitance of the materials. Figure 4a represents the cyclic voltammetry curve for $La_{1-x}K_xFeO_{3-\delta}$ (x = 0, 0.3, 0.4, 0.5) with increasing K concentration. The $Fe^{4+/3+}$ and $Fe^{3+/2+}$ redox peaks appear shifted to a lower potential linearly. For example, in undoped $LaFeO_3$ the $Fe^{3+/2+}$ redox

couple appears at −0.84 V, in $La_{0.7}K_{0.3}FeO_{3-\delta}$ it appears at −0.64 V, and in $La_{0.5}K_{0.5}FeO_{3-\delta}$ it appears at −0.59 V. Similarly, the $Fe^{4+/3+}$ couple appears at −0.85 V in $La_{0.5}K_{0.5}FeO_{3-\delta}$ and at −0. 89 V in $La_{0.7}K_{0.3}FeO_{3-\delta}$, and did not appear up to −1 V for undoped $LaFeO_3$. Thus, the inductive internal potential arises due to alternation of La and K layers over the Fe−O octhedra (as shown in Figure 1c), which makes the $Fe^{4+/3+}$ redox couple accessible for electrochemical performances. The cyclic voltammetry curves for $La_{1-x}K_xFeO_{3-\delta}$ (x = 0, 0.3, 0.4, 0.5) with different scan rates

are shown in Figure 4b−d, respectively. For the $x = 0.3$ composition, $La_{0.7}K_{0.3}Fe_{0.55}^{4+}Fe_{0.46}^{3+}O_{2.97}$, with almost equal concentrations of Fe^{4+} and Fe^{3+} states, both $Fe^{4+/3+}$ and $Fe^{3+/2+}$ redox peaks seem to operate in a very close voltage range, representing a clean diffusion-controlled behavior of the electrode. However, a low capacity output resulted for the $La_{0.7}K_{0.3}Fe_{0.55}^{4+}Fe_{0.46}^{3+}O_{2.97}$ electrode. The quasi-rectangular shape of the curve suggests the dominance of pseudocapacitance behavior over EDLC. The specific capacitance C (F/g) was calculated to understand the electrochemical performance of the working electrode, as represented by eq 1.
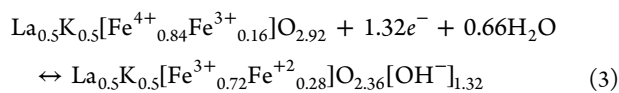
$$C_{sp} = \frac{\int I(V)dV}{mV\nu} \quad (1)$$

where $I(A)$ is the cathodic current, ν (V/s) is the scan rate, m (g) is the mass of active material, and V (V) is the sweep potential window.[35]

The gravimetric capacitance of $La_{1-x}K_xFeO_{3-\delta}$ ($x = 0, 0.1, 0.2, 0.3, 0.4, 0.5$) materials from the cyclic voltammetry curve at a scan rate of 1 mV/s was found to be 95, 113, 143, 203, 394, and 662 F/g, respectively. The capacitance of $La_{0.5}K_{0.5}FeO_{2.92}$, which contains almost 84% Fe in the Fe^{4+} oxidation state as confirmed by XPS and iodometry titration study, was found to be ~662 F/g, suggesting more than one electron or anion transfer per molecule. In aqueous KOH electrolyte with predominant OH^- transportation, the redox reaction pseudocapacitive storage can be represented as

$$La_{1-x}K_x[Fe^{4+}Fe^{3+}]O_{3-\delta} + 2ye^- + yH_2O$$
$$\leftrightarrow La_{1-x}K_x[Fe^{3+/2+}]O_{3-y-\delta}[OH^-]_{2y} \quad (2)$$
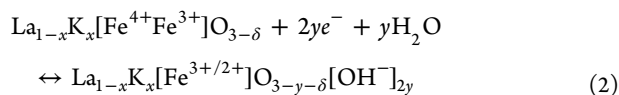
Thus, formation of $La_{1-x}K_x[Fe^{3+/2+}]O_{3-y-\delta}[OH^-]_{2y}$ results in pseudocapacitance through OH^- intercalation coupled with surface adsorption. For $y = 0.5$, with the intercalation of one OH^- coupled with $1e^-$ charge transfer, the theoretical capacity of $La_{0.5}K_{0.5}FeO_{2.92}$ should be ~500 F/g, and therefore with the observation of ~662 F/g capacity of the electrode, the equivalent charge transfer of $1.32e^-$ or OH^-/H_2O transport/transfer takes place per molecule of $La_{0.5}K_{0.5}FeO_{2.92}$.

Thus, for $La_{0.5}K_{0.5}[Fe_{0.84}^{4+}, Fe_{0.16}^{3+}]O_{2.92}$, the redox reaction can be represented as

$$La_{0.5}K_{0.5}[Fe^{4+}_{0.84}Fe^{3+}_{0.16}]O_{2.92} + 1.32e^- + 0.66H_2O$$
$$\leftrightarrow La_{0.5}K_{0.5}[Fe^{3+}_{0.72}Fe^{+2}_{0.28}]O_{2.36}[OH^-]_{1.32} \quad (3)$$

To understand the electrochemical kinetics of the $La_{1-x}K_xFeO_{3-\delta}$ ($x = 0, 0.3, 0.5$) sample, a plot of the anodic and cathodic peak currents with respect to the square root of the scan rate is plotted in Figure 4e. The linear fitting of these plots represents a semi-infinite diffusion-controlled process. The kinetics of the electrode can be examined with the help of the diffusion coefficient. Determination of the diffusion coefficient of those electrodes was done using Randles−Sevick equation.[36]

$$i_p = 2.686 \times 10^5 \times n^{3/2}AD^{1/2}C_o\nu^{1/2} \quad (4)$$

where i_p is the peak current (A), n is the number of electrons transferred in the redox event (usually 1), A is the electrode area in cm^2, D is the diffusion coefficient in cm^2/s, C_o is the OH^- ion concentration in mol/cm^3, and ν is the scan rate in V/s. The diffusion coefficients of OH^- calculated using eq 4 at 1 mV/s are presented in Table 1. For $La_{1-x}K_xFeO_{3-\delta}$ ($x = 0$,

Table 1. Determination of the Diffusion Coefficient

sample	diffusion coefficient of the anodic peak current (D_a) (cm^2/s)	diffusion coefficient of the cathodic peak current (D_c) (cm^2/s)
$LaFeO_3$	5.827×10^{-8}	5.998×10^{-8}
$La_{0.7}K_{0.3}FeO_{3-\delta}$	4.554×10^{-7}	3.889×10^{-7}
$La_{0.5}K_{0.5}FeO_{3-\delta}$	9.806×10^{-7}	7.711×10^{-7}

0.3, 0.4, 0.5) anode materials, the forward reaction is a charging and backward reaction discharging process. During the charging process, H_2O and e^- react at the electrode surface with OH^- that are diffused through the surface to the lattice.[37,38] During discharge, H_2O is exchanged through the lattice resulting in recreation of the initial structure.

The area under the curve from the CV plot represents the total charge stored through faradic and nonfaradic reactions occurring on the electrode surface. The current behavior generally follows the power law and is related to the scan rate by the following equation

$$i = a\nu^b \quad (5)$$

where a and b are the variables that govern the nature of intercalation, i is the current (A), and θ is the scan rate (V/s). The value of b lies between 0.5 and 1, $b = 0.5$ stands for the diffusion control reaction or battery type behavior, and $b = 1$ stands for the diffusion control faradic process involving charge transfer with surface/subsurface atoms.[39] The b values for the $La_{0.5}K_{0.5}FeO_{3-\delta}$ sample were found to be varying linearly with the scan rates at different potentials ranging from −0.2 to −0.8 V as shown in Supporting Figure S2-a,b. As shown in Figure 5a, in the charging process of the anode material at −0.4 V, the b value was found to be 0.57, suggesting the dominance of the diffusion control process; except at −0.4 V, for other potentials the b values were found to be above 0.8, suggesting the dominance of the faradic process over surface couples' redox-mediated capacitance behavior. Similarly, in the discharging process, b values were found to higher than 0.85, suggesting the redox pseudocapacitive process from charge transfer with surface/subsurface atoms (Supporting Figure S2-a,b). The b values for $La_{0.5}K_{0.5}FeO_{3-\delta}$ electrode were varied differently in two different regions, (1) ≤10 mV/s and (2) ≥10 mV/s, in the plot of the log(peak current (A)) vs log(scan rate (mV/s)) as shown in Figure 5b. The b values for cathodic and anodic diffusion are 1 and 0.98, respectively, below 10 mV/s, suggesting rapid surface control kinetics, and the b values for cathodic and anodic diffusion are 0.87 and 0.7 above 10 mV/s, suggesting a resistance at high scan rates.

Similarly, the voltammetry sweep rate dependence on the current response can distinguish the capacitive contribution to the current response quantitatively. The current response at a fixed potential is envisaged as the combination of two separate mechanisms, surface capacitive effects, and diffusion-controlled insertion.[40,41]

$$i(\nu) = K_1\nu + K_2\nu^{1/2} \quad (6)$$

For more understanding, eq 6 can be rearranged to

$$\frac{i(\nu)}{\nu^{1/2}} = \frac{K_1}{\nu^{1/2}} + K_2 \quad (7)$$

$K_1\nu$ and $K_2\nu^{1/2}$ represent the current contributions from the surface capacitive effects and the diffusion-controlled intercalation process, respectively. Thus, after the determination of
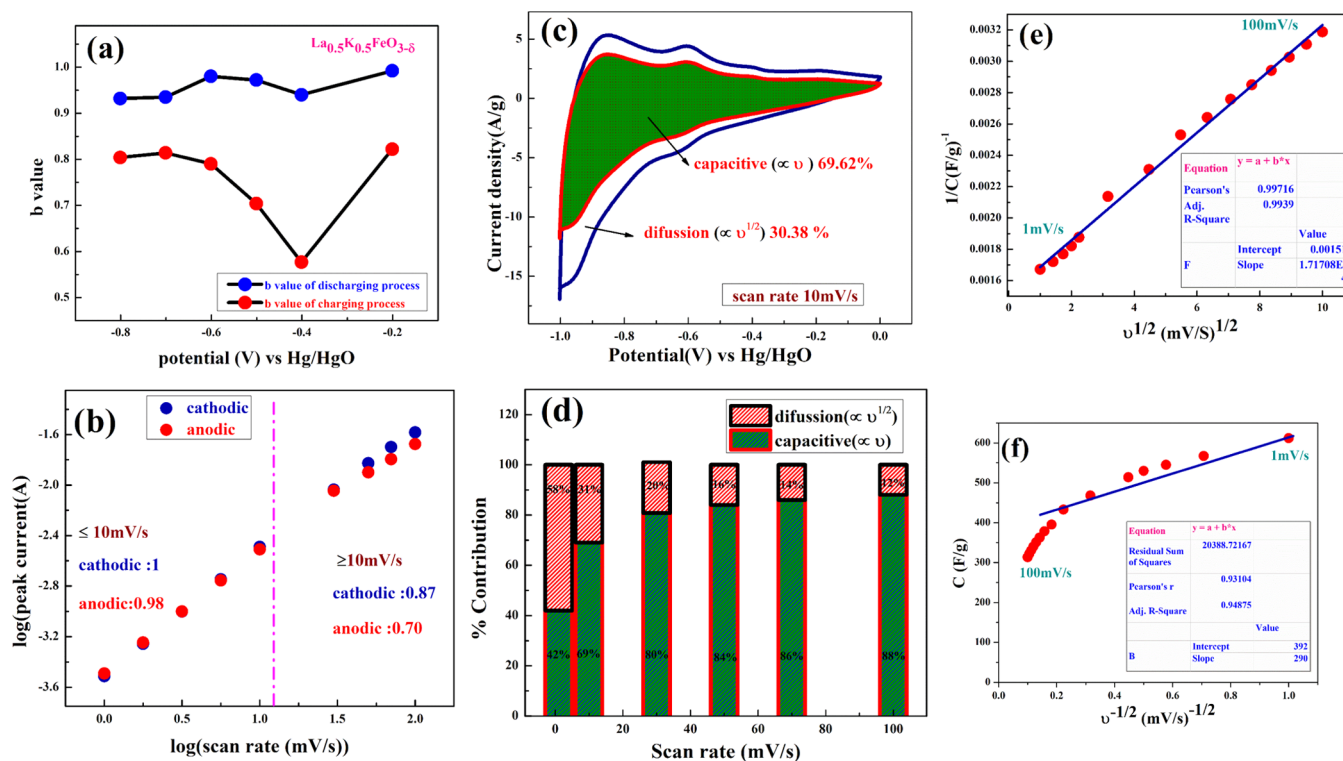
Figure 5. (a) *b* Values at different potentials of La$_{0.5}$K$_{.5}$FeO$_{3-\delta}$ in the charging and discharging processes at different potentials; (b) plot of log(peak current) vs log(scan rate); (c) capacitive and diffusion control process of the La$_{0.5}$K$_{.5}$FeO$_{3-\delta}$ electrode at 10 mV/s; (d) capacitive and diffusion control percentage with different scan rates at the discharge peak potential (−0.96 V); and (e, f) Trasatti plot at a scan rate of 100 to 1 mV/s for the charge−discharge process.

k_1 and k_2, we can quantify the fraction of the current due to each of these contributions at specific potentials. With the linear fitting of the $i(\nu)/\nu^{1/2}$ vs $1/\nu^{1/2}$ plot with different scan rates for the La$_{0.5}$K$_{0.5}$FeO$_{3-\delta}$ sample, k_1 and k_2 values are determined from the slope and intercept of the *y* axis, respectively. The representative curve of $i(\nu)/\nu^{1/2}$ vs $\nu^{1/2}$ for the La$_{0.5}$K$_{0.5}$FeO$_{3-\delta}$ sample is shown in Supporting Figure S3a,b.

The contribution of surface capacitance (69.62%) and diffusion-controlled interaction (30.38%) was found for the La$_{0.5}$K$_{0.5}$FeO$_{3-\delta}$ electrode at the operating potential of −0.6 V with a scan rate of 10 mV/s as shown in Figure 5c. The surface capacitance and diffusion-controlled interaction participations are varied linearly with varying scan rates. The surface capacitive and diffusion control contributions are 42 and 58%, respectively, at −0.6 V with a scan rate of 1 mV/s. The surface capacitive contribution increases with increasing scan rate; i.e., the surface capacitive contribution and diffusion control contribution were found to be 88 and 12%, respectively, at 100 mV/s as shown in Figure 5d.

According to Trasatti, the total specific capacitance is the sum of intercalative (inner) and outer surface capacitance values of the electrode. It can be expressed as

$$C_{total} = C_{in} + C_{out} \tag{8}$$

The specific capacitance contributed from the inner and outer surfaces of the electrode is dependent upon the scan rate (Figure 5e). The *y*-intercept of the linear fit of the $1/q$ vs $\nu^{1/2}$ plot at $\nu = 0$ represents the total amount of charge stored in the electrode. In Figure 5f, the *y*-intercept of the linear fit of the q vs $\nu^{-1/2}$ plot at $\nu = \infty$ corresponds to the amount of charge stored at the outer surface of the electrode.[42] Applying

the Trassati plot outcome, it can be concluded that the total capacitance value ($C_{total} = 662$ F/g) of La$_{0.5}$K$_{0.5}$FeO$_{3-\delta}$ has an intercalative inner surface contribution (C_{in}) equivalent to 359 F/g and outer surface contribution (C_{out}) equivalent to 303 F/g.

The charge−discharge measurement (potential (V) vs time (t)) was carried out at a constant current by chronopotentiometry. The gravimetric capacitance value was calculated from the potential (V) vs time (t) plot by using the following equation

$$C = \frac{I\Delta t}{mV} \tag{9}$$

where I (A) is the applied constant current, Δt (s) is the discharge time, m (g) is the active mass, and V represents the operating potential window.[43]

The gravimetric capacitance values of the La$_{1-x}$K$_x$FeO$_{3-\delta}$ (x = 0, 0.1, 0.2 0.3, 0.4, 0.5) electrode from the charge−discharge plot are shown in Figure 6a, and at a current rate of 1 A/g their values were found to be 101, 117, 148, 226, 389, and 619 F/g, respectively. The gravimetric capacitance values in Figure 6b are found to be 619, 347, 188, 121, and 65 F/g, respectively, at a constant current of 1, 2, 3, 5, and 10 A/g for the La$_{0.5}$K$_{0.5}$FeO$_{3-\delta}$ electrode. The capacitance performance for different cycle numbers of the La$_{0.5}$K$_{0.5}$FeO$_{3-\delta}$ electrode is shown in Figure 6c. Up to 88.5% capacitive retention and Coulombic efficacy (95%) was obtained for continuous 5000 cycles of charge/discharge for the La$_{0.5}$K$_{0.5}$FeO$_{3-\delta}$ electrode at 5 A/g constant current as shown in Figure 6d. The electrochemical impedance spectroscopy (EIS) measurement was carried out at an applied AC voltage of 10 mV from 1 MHz to 0.1 Hz range and is shown by the Nyquist plot in
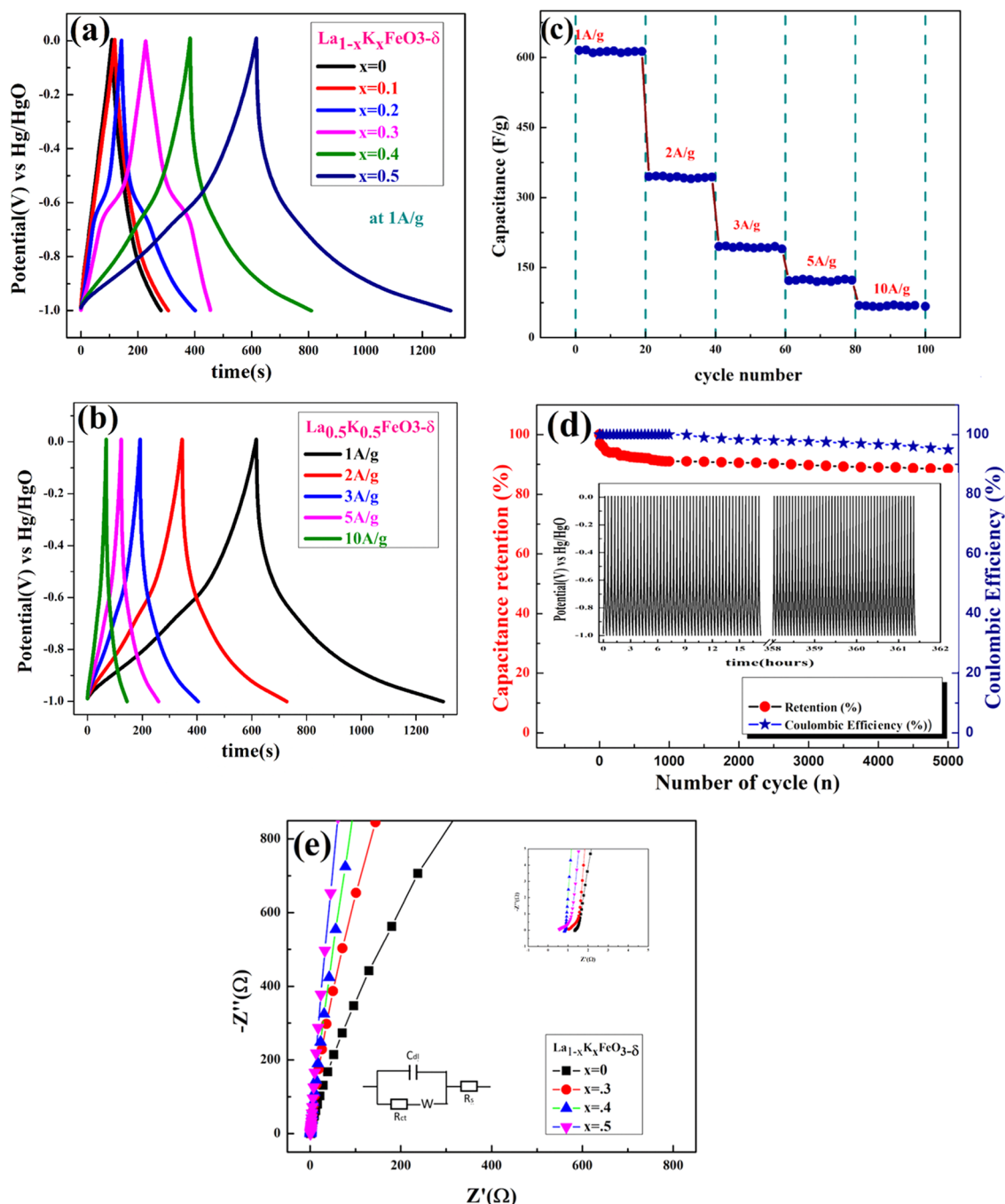
Figure 6. (a) Charge−discharge plot (*V* vs time) of the La$_{1-x}$K$_x$FeO$_{3-\delta}$ (*x* = 0, 0.3, 0.4, 0.5) electrode at 1 A/g; (b) charge−discharge plot (potential (*V*) vs time (*t*)) of the La$_{0.5}$K$_{0.5}$FeO$_{3-\delta}$ electrode; (c) capacitance performance of the La$_{0.5}$K$_{0.5}$FeO$_{3-\delta}$ 2 M KOH electrolyte at different constant currents; (d) capacitive retention and Coulombic efficacy with cycle number; and (e) impedance spectroscopy (EIS) at 10 mV applied voltage from 1 MHz to 0.1 Hz.

Figure 6e for the La$_{1-x}$K$_x$FeO$_{3-\delta}$ (*x* = 0, 0.3, 0.4, 0.5) electrodes. The specific impedance contribution is mainly attributed to the impedance distributions over the electric series resistance (R_s), charge transfer resistance (R_{ct}), and Warburg impedance (R_w). The higher frequency resistance of the La$_{1-x}$K$_x$FeO$_{3-\delta}$ electrode gradually decreases with increasing K ion substitution in the sample, as the electronic conductivities of the samples increase with increasing K doping. The lower-frequency data represent the Warburg diffusion resistance, and for La$_{1-x}$K$_x$FeO$_{3-\delta}$ (*x* = 0, 0.3, 0.4, 0.5) samples, the straight line in the low-frequency region is

close to 90° (very close to the −$Z''(\Omega)$ axis) and the horizontal line represents the characteristic of pseudocapacitance behavior of the La$_{0.5}$K$_{0.5}$FeO$_{3-\delta}$ electrode. This also represents fast OH$^-$ ion diffusion in the porous structure.

Two-Electrode Test. To understand the real charge storage behavior of La$_{0.5}$K$_{0.5}$FeO$_{3-\delta}$ relative to AC (activated carbon), two-electrode ASC (asymmetry supercapacitor) measurements have been conducted in 2 M KOH. To determine the maximum specific capacitance during full test, the storage capacity of the positive and negative electrodes needs to be balanced as per the following equation
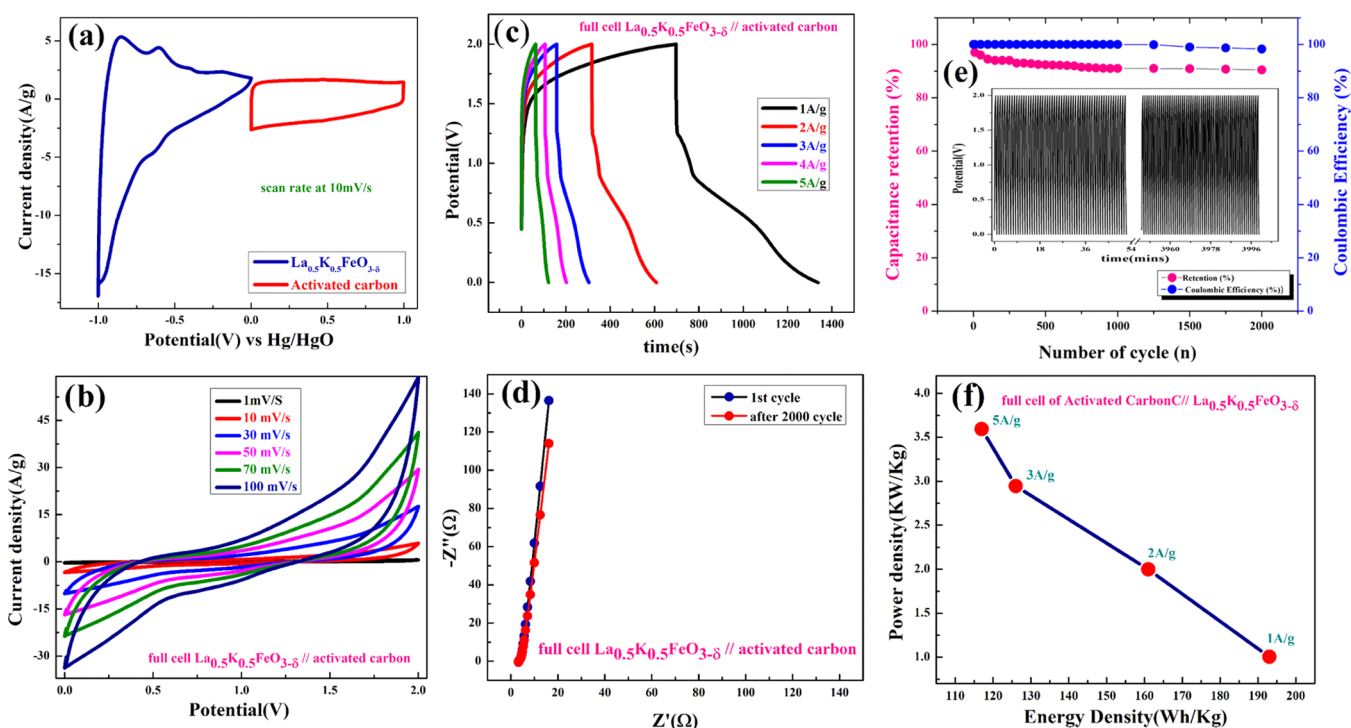
Figure 7. Full-cell (ASC) performances of activated carbon vs the La$_{0.5}$ K$_{0.5}$FeO$_{3-\delta}$ electrode. (a) CV of individual electrodes at 10 mV/s with respect to the Hg/HgO electrode; (b) CV at different scan rates of ASCs; (c) charge−discharge plot; (d) EIS plot at 10 mV applied voltage; (e) capacitance retention and Coulombic efficiency with 2000 cycles at 5 A/g constant current of the full cell; and (f) Ragone plot of the ASCs.

$$\frac{1}{C_{total}} = \frac{1}{C_{positive}} + \frac{1}{C_{negative}} \qquad (10)$$

For balancing the charge storage capacity of the cell, the mass ratio (m^+/m^-) of the positive and negative electrode materials was measured using the following equation

$$\frac{m^+}{m^-} = \frac{C_- \times \Delta E_-}{C_+ \times \Delta E_+} \qquad (11)$$

where m^+, m^-, C_+, C_-, ΔE_+, and ΔE_- are the mass, specific capacitance, and potential window of the positive and negative electrodes, respectively, estimated by the three-electrode measurement.[36,37]

Figure 7a shows the CV at 10 mV/s scan rate where the used AC (activated carbon) acts as the positive electrode and La$_{0.5}$K$_{0.5}$FeO$_{3-\delta}$ acts as the negative electrode. The calculated mass ratio (m^+/m^-) was found to be 1:2.23 for the asymmetric cell, and the weight of the active materials was taken to be 3.3 mg (excluding the weight of acetylene black and PVDF). Figure 7b demonstrates the CV curve of the two electrodes La$_{0.5}$K$_{0.5}$FeO$_{3-\delta}$//AC in ASC mode at different scan rates, ranging from 1 to 100 mV/s in the potential window of 2 V, to assess the possible change in the oxidation state of Fe from Fe^{2+} to Fe^{4+}. Figure 7c shows the charge−discharge curve plotted for measuring the capacitance of the electrode; the capacitance value was calculated using eq 9. The capacitance values for the La$_{0.5}$K$_{0.5}$FeO$_{3-\delta}$ electrodes were found to be 348, 290, 228, and 147 F/g at current densities of 1, 2, 3, and 5 A/g, respectively. Figure 7d shows the EIS plot (Nyquist) in the frequency range 1 MHz to 0.1 Hz at 10 mV applied voltage, confirming the superior charge transfer and higher capacitance of La$_{0.5}$K$_{0.5}$FeO$_{3-\delta}$//AC in full-cell mode. Figure 7e shows that the Coulombic efficiency of the two-electrode full cell is

reduced only by 3%, with a higher capacity retention close to 90.5% of its initial value after 2000 cycles at a constant current of 5 A/g. The specific energy and specific power of the asymmetric capacitors were calculated using the following equations

$$E \; (\text{Wh/kg}) = \frac{1}{2}\frac{C_{ASCs}}{3.6}V^2 \qquad (12)$$

$$P \; (\text{W/kg}) = \frac{E*3600}{t_{dis}} \qquad (13)$$

where C_{ASCs} is the specific capacitance, V is the operating voltage, and t_{dis} is the discharge time.[37]

Figure 7f shows the plot of specific energy vs specific power with different constant current rates. The resultant values show the highest specific energy of 193 Wh/kg at 1 A/g current density and a specific power of ~1004 W/kg. The maximum specific power of ~3594 W/kg was obtained when the specific energy was reduced to ~117 Wh/kg at 5 A/g current density.

CONCLUSIONS

In summary, it can be concluded that by using an induced interlayer potential by altering the La^{3+} and K$^+$ layer in La$_{1-x}$K$_x$FeO$_{3-\delta}$, Fe$^{4+/3+}$ and Fe$^{3+/2+}$ redox energies can be tuned and made accessible to envisage a higher capacity (662 F/g equivalent to 1.32e$^-$/OH$^-$ diffusion) for the La$_{0.5}$K$_{0.5}$FeO$_{2.92}$ electrode. The higher b values (>0.8) obtained for the diffusion-controlled reaction suggest a high faradic pseudocapacitive contribution to the electrode. Even with the Trassati plot, a higher degree of inner layer contribution, 54% (C_{in} = 359 F/g), to the total capacitance (C_{total} = 662 F/g) was obtained for the La$_{0.5}$K$_{0.5}$FeO$_{3-\delta}$ electrode. Up to 88.6% capacitive retention and Coulombic efficacy (95%) was

obtained after continuous 5000 cycles of charge/discharge, and a maximum specific power of ∼3594 W/kg was obtained when the specific energy reached ∼117 Wh/kg at 5 A/g of current density for the $La_{0.5}K_{0.5}FeO_{3-\delta}$ electrode in the two-electrode $La_{0.5}K_{0.5}FeO_{3-\delta}//AC$ full-cell mode, with the remarkable stability of the electrode making the $La_{0.5}K_{0.5}FeO_{3-\delta}$ electrode suitable as a negative electrode for pseudocapacitor applications.

■ ASSOCIATED CONTENT

ⓈⒾ Supporting Information

The Supporting Information is available free of charge at https://pubs.acs.org/doi/10.1021/acsomega.1c03902.

> Enlarged image of powder XRD plot of $La_{1-x}K_xFeO_3$ (x = 0, 0.1, 0.2, 0.3, 0.4, 0.5) showing peak shifting of (002) diffraction peak; plot shows linear relationship of $\log(\nu)$ vs $\log(i)$, slope represent b value according to power law; and capacitive and diffusion control processes contribution can be distinguish from applying equation (PDF)

■ AUTHOR INFORMATION

Corresponding Author

Preetam Singh − *Department of Ceramic Engineering, Indian Institute of Technology (Banaras Hindu University), Varanasi, Uttar Pradesh 221005, India;* ⊙ orcid.org/0000-0002-7590-3576; Phone: 91-9473720659; Email: preetamsingh.cer@itbhu.ac.in, preetamchem@gmail.com

Authors

Rakesh Mondal − *Department of Ceramic Engineering, Indian Institute of Technology (Banaras Hindu University), Varanasi, Uttar Pradesh 221005, India*

Neeraj Kumar Mishra − *Department of Ceramic Engineering, Indian Institute of Technology (Banaras Hindu University), Varanasi, Uttar Pradesh 221005, India*

Thandavarayan Maiyalagan − *Electrochemical Energy Laboratory, Department of Chemistry, SRM Institute of Science and Technology, Kattankulathur 603203 Tamilnadu, India;* ⊙ orcid.org/0000-0003-3528-3824

Asha Gupta − *Department of Chemistry, Indian Institute of Technology (Banaras Hindu University), Varanasi, Uttar Pradesh 221005, India;* ⊙ orcid.org/0000-0003-1386-2382

Complete contact information is available at:
https://pubs.acs.org/10.1021/acsomega.1c03902

Notes

The authors declare no competing financial interest.

■ ACKNOWLEDGMENTS

■ REFERENCES

(1) Simon, P.; Gogotsi, Y. Materials for electrochemical capacitors. *Nat. Mater.* **2008**, 7, 845−854.

(2) Hall, P. J.; Mirzaeian, M.; Fletcher, S. I. l.; Sillars, F. B.; Rennie, A. J. R.; Shitta-Bey, G. O.; Wilson, G.; Crudenb, A.; Carter, R. Energy storage in electrochemical capacitors: designing functional materials to improve performance. *Energy Environ. Sci.* **2010**, 3, 1238−1251.

(3) Goodenough, J. B. *Basic Research Needs for Electrical Energy Storage: Report of the Basic Energy Sciences Workshop on Electrical Energy Storage*; Office of Basic Energy Sciences, DOE, 2007.

(4) Gogotsi, Y. What Nano Can Do for Energy Storage. *ACS Nano* **2014**, 8, 5369−5371.

(5) Jiang, H.; Yang, L.; Li, C.; Yan, C.; Leec, P. S.; Ma, J. High−rate electrochemical capacitors from highly graphitic carbon−tipped manganese oxide/mesoporous carbon/manganese oxide hybrid nanowires. *Energy Environ. Sci.* **2011**, 4, 1813−1819.

(6) Goodenough, J. B.; Park, K. S. The Li-Ion Rechargeable Battery: A Perspective. *J. Am. Chem. Soc.* **2013**, 135, 1167−1176.

(7) Conway, B. E.; Pell, W. G. Double-layer and pseudocapacitance types of electrochemical capacitors and their applications to the development of hybrid devices. *J. Solid State Electrochem.* **2003**, 7, 637−644.

(8) Gogotsi, Y.; Penner, R. M. Energy Storage in Nanomaterials−Capacitive, Pseudocapacitive, or Battery-like? *ACS Nano* **2018**, 12, 2081−2083.

(9) Forghani, M.; Donne, S. W. Method comparison for deconvoluting capacitive and pseudo-capacitive contributions to electrochemical capacitor electrode behaviour. *J. Electrochem. Soc.* **2018**, 165, A664−A673.

(10) Augustyn, V.; Simon, P.; Dunn, B. Pseudocapacitive oxide materials for high-rate electrochemical energy storage. *Energy Environ. Sci.* **2014**, 7, 1597−1614.

(11) Jabeen, N.; Xia, Q.; Savilov, S. V.; Aldoshin, S. M.; Yu, Y.; Xia, H. Enhanced Pseudocapacitive Performance of α-MnO_2 by Cation Preinsertion. *ACS Appl. Mater. Interfaces* **2016**, 8, 33732−33740.

(12) Devaraj, S.; Munichandraiah, N. Effect of Crystallographic Structure of MnO_2 on Its Electrochemical Capacitance Properties. *J. Phys. Chem. C* **2008**, 112, 4406−4417.

(13) Liu, K. C.; Anderson, M. A. Porous Nickel Oxide/Nickel Films for Electrochemical Capacitors. *J. Electrochem. Soc.* **1996**, 143, 124−130.

(14) Lee, H. Y.; Goodenough, J. B. Ideal supercapacitor behaviour of amorphous $V_2O_{5}.nH_2O$ in potassium chloride (KCl) aqueous solution. *J. Solid State Chem.* **1999**, 148, 81−84.

(15) Gao, Y.; Chen, S.; Cao, D.; Wang, G.; Yin, J. Electrochemical capacitance of Co_3O_4 nanowire arrays supported on nickel foam. *J. Power Sources* **2010**, 195, 1757−1760.

(16) Xia, X. H.; Tu, J. P.; Wang, X. L.; Gu, C. D.; Zhao, X. B. Mesoporous Co_3O_4 monolayer hollow-sphere array as electrochemical pseudocapacitor material. *Chem. Commun.* **2011**, 47, 5786−5788.

(17) Wang, S. Y.; Ho, K. C.; Kuo, S. L.; Wu, N. L. Investigation on capacitance mechanisms of Fe_3O_4 electrochemical capacitors. *J. Electrochem. Soc.* **2006**, 153, A75−A80.

(18) Liu, X. Y.; Zhang, Y. Q.; Xia, X. H.; Shi, S. J.; Lu, Y.; Wang, X. L.; Gu, C. D.; Tu, J. P. Self-assembled porous $NiCo_2O_4$ heterostructure array for electrochemical capacitor. *J. Power Sources* **2013**, 239, 157−163.

(19) Mefford, J. T.; Hardin, W. G.; Dai, S.; Johnston, K. P.; Stevenson, K. J. Anion charge storage through oxygen intercalation in $LaMnO_3$ perovskite pseudocapacitor electrodes. *Nat. Mater.* **2014**, 13, 726−732.

(20) (a) Alexander, C. T.; Mefford, J. T.; Saunders, J.; Forslund, R. P.; Johnston, K. P.; Stevenson, K. J. Anion-Based Pseudocapacitance of the Perovskite Library $La_{1-x}Sr_xBO_{3-\delta}$ (B = Fe, Mn, Co). *ACS Appl. Mater. Interfaces* **2019**, 11, 5084−5094. (b) Nan, H.-S.; Hu, X.-Y.; Tian, H.-W. Recent advances in perovskite oxides for anion-intercalation supercapacitor: A review. *Mater. Sci. Semicond. Process.* **2019**, 94, 35−50.

(21) Mefford, J. T.; Rong, X.; Abakumov, A. M.; Hardin, W. G.; Dai, S.; Kolpak, A. M.; Johnston, K. P.; Stevenson, K. J. Water electrolysis on La$_{1-x}$Sr$_x$CoO$_{3-\delta}$ perovskite electrocatalysts. *Nat. Commun.* **2016**, *7*, No. 11053.

(22) Shao, T.; You, H.; Zhai, Z.; Liu, T.; Li, M.; Zhang, L. Hollow spherical LaNiO$_3$ supercapacitor electrode synthesized by a facile template-free method. *Mater. Lett.* **2017**, *201*, 122−124.

(23) Li, Z.; Zhang, W.; Yuan, C.; Su, Y. Controlled synthesis of perovskite lanthanum ferrite nanotubes with excellent electrochemical properties. *RSC Adv.* **2017**, *7*, 12931−12937.

(24) Zhang, B.; Yu, C.; Li, Z. Enhancing the Electrochemical Properties of LaCoO$_3$ by Sr-Doping, rGO-Compounding with Rational Design for Energy Storage Device. *Nanoscale Res. Lett.* **2020**, *15*, No. 184.

(25) Cao, Y.; Lin, B.; Sun, Y.; Yang, H.; Zhang, X. Symmetric/ Asymmetric Supercapacitor Based on the Perovskite-type Lanthanum Cobaltate Nanofibers with Sr-substitution. *Electrochim. Acta* **2015**, *178*, 398−406.

(26) Tomar, A. K.; Joshi, A.; Atri, S.; Singh, G.; Sharma, R. K. Zero-dimensional ordered Sr$_2$CoMoO$_{6-\delta}$ double perovskite as high-rate anion intercalation pseudocapacitance. *ACS Appl. Mater. Interfaces* **2020**, *12*, 15128−15137.

(27) Cao, Y.; Lin, B.; Sun, Y.; Yang, H.; Zhang, X. Structure, morphology and electrochemical properties of La$_x$Sr$_{1-x}$Co$_{0.1}$Mn$_{0.9}$O$_{3-\delta}$ perovskite nanofibers prepared by electro-spinning method. *J. Alloys Compd.* **2015**, *624*, 31−39.

(28) (a) Eatough, M. O.; Ginley, D. S.; Morosin, B.; Venturini, E. L. Orthorhombic-tetragonal phase transition in high-temperature super-conductor YBa$_2$Cu$_3$O$_7$. *Appl. Phys. Lett.* **1987**, *51*, 367. (b) Jang, W.-J.; Mori, H.; Watahiki, M.; Tajima, S.; Koshizuka, N.; Tanaka, S. *J. Solid State Chem.* **1996**, *122*, 371−375. Structure Analysis of the Twin-Free Orthorhombic YBa$_2$Cu$_3$O$_{7-x}$ Single Crystals

(29) (a) Chaillout, C.; Cheong, S. W.; Fisk, Z.; Lehmann, M. S.; Marezio, M.; Morosin, B.; Schirber, J. E. The crystal structure of superconducting La$_2$CuO$_{4.032}$ by neutron diffraction. *Phys. C* **1989**, *158*, 183−191. (b) Goodenough, J. B.; Zhou, J.-S. Orbital ordering in orthorhombic perovskites. *J. Mater. Chem.* **2007**, *17*, 2394−2405.

(30) Kumada, N.; Kinomura, N.; Sleight, A. W. CsLaNb$_2$O$_7$. *Acta Crystallogr., Sect. C: Cryst. Struct. Commun.* **1996**, *52*, 1063−1065.

(31) Song, S.-H.; Ahn, K.; Kanatzidis, M. G.; Alonso, J. A.; Cheng, J.-G.; Goodenough, J. B. Effect of an Internal Electric Field on the Redox Energies of A*Ln*TiO$_4$ (*A* = Na or Li, *Ln* = Y or Rare-Earth). *Chem. Mater.* **2013**, *25*, 3852−3857.

(32) Shannon, R. D. Revised effective ionic radii and systematic studies of interatomic distances in halides and chalcogenides. *Acta Crystallogr., Sect. A: Cryst. Phys., Diffr, Theor. Gen. Crystallogr.* **1976**, *32*, 751−767.

(33) Qian, F.; Li, X.; Tang, L.; Lai, S. K.; Lu, C.; Lau, S. P. Potassium doping: Tuning the optical properties of graphene quantum dots. *AIP Adv.* **2016**, *6*, No. 075116.

(34) Ghaffari, M.; Liu, T.; Huang, H.; Tan, O. K.; Shannon, M. Investigation of local structure effect and X-ray absorption character-istics (EXAFS) of Fe (Ti) K-edge on photocatalyst properties of SrTi$_{(1-x)}$Fe$_x$O$_{(3-\delta)}$. *Mater. Chem. Phys.* **2012**, *136*, 347−357.

(35) Lang, X.; Mo, H.; Hu, X.; Tian, H. Supercapacitor performance of perovskite La$_{1-x}$Sr$_x$MnO$_3$. *Dalton Trans.* **2017**, *46*, 13720−13730.

(36) Zhang, X.; Zheng, J. Controllable synthesis of highly active Au@Ni nanocatalyst supported on graphene oxide for electrochemical sensing of hydrazine. *Appl. Surf. Sci.* **2019**, *493*, 1159−1166.

(37) Mathis, T. S.; Kurra, N.; Wang, X.; Pinto, D.; Simon, P.; Gogotsi, Y. Energy Storage Data Reporting in Perspective—Guidelines for Interpreting the Performance of Electrochemical Energy Storage Systems. *Adv. Energy Mater.* **2019**, *9*, No. 1902007.

(38) Hu, N.; Gong, W. H.; Huang, L.; Shen, P. K. Ultrahigh energy density asymmetric electrochemical capacitors based on flower-like ZnO/Co$_3$O$_4$ nanobundle arrays and stereotaxically constricted grapheme. *J. Mater. Chem. A* **2019**, *7*, 1273−1280.

(39) Yang, P.; Wu, Z.; Jiang, Y.; Pan, Z.; Tian, W.; Jiang, L.; Hu, L. Fractal (Ni$_x$Co$_{1-x}$)$_9$Se$_8$ Nanodendrite Arrays with Highly Exposed (01$\bar{1}$) Surface for Wearable, All-Solid-State Supercapacitor. *Adv. Energy Mater.* **2018**, *8*, No. 1801392.

(40) Brezesinski, T.; Wang, J.; Tolbert, S. H.; Dunn, B. Ordered mesoporous alpha-MoO$_3$ with iso-oriented nanocrystalline walls for thin-film pseudocapacitors. *Nat. Mater.* **2010**, *9*, 146−151.

(41) Wang, J. J.; Polleux, J. L.; Lim, J.; Dunn, B. Pseudocapacitive Contributions to Electrochemical Energy Storage in TiO$_2$ (Anatase) Nanoparticles. *J. Phys. Chem. C* **2007**, *111*, 14925−14931.

(42) Singh, A. K.; Sarkar, D.; Karmakar, K.; Mandal, K.; Khan, G. G. High-Performance Supercapacitor Electrode Based on Cobalt Oxide−Manganese Dioxide−Nickel Oxide Ternary 1D Hybrid Nanotubes. *ACS Appl. Mater. Interfaces* **2016**, *8*, 20786−20792.

(43) Pal, B.; Yang, S.; Ramesh, S.; Thangadurai, V.; Jose, R. Electrolyte selection for supercapacitive devices: a critical review. *Nanoscale Adv.* **2019**, *1*, 3807−3835.